Localized layers of turbulence in vertically-stratified plane Poiseuille flow

Joris Labarbe, P Le Gal, U Harlander, S Le Dizès, B Favier

Localized layers of turbulence in vertically-stratified plane Poiseuille flow

J. Labarbe[1]†, P. Le Gal[1], U. Harlander[2], S. Le Dizès[1] and B. Favier[1]

[1]Aix Marseille Univ., CNRS, Centrale Marseille, IRPHE, Marseille, France

[2]Department of Aerodynamics and Fluid Mechanics, Brandenburg University of Technology, Cottbus-Senftenberg, Germany

(Received xx; revised xx; accepted xx)

This article presents a numerical analysis of the instability developing in horizontal plane Poiseuille flow, when stratification extends along the direction orthogonal to the plane of shear. Our study builds up on the previous work that originally detected the linear instability of such configuration, by means of experiments, theoretical analysis and numerical simulations (Le Gal *et al.* 2021). We extend hereafter this former investigation beyond linear theory, investigating nonlinear regimes with direct numerical simulations. We notice a tendency for the flow to lose its vertical homogeneity through a point of secondary bifurcation, due to harmonic resonances, and further describe this symmetry-breaking mechanism in the vicinity of the instability threshold. When departing away from this limit, we observe a series of bursting events that break down the flow into disordered motions driven by localized shear instabilities. This intermittent dynamics leads to the coexistence of localized layers of stratified turbulence surrounded by quiescent regions of meandering waves.

Key words:

1. Introduction

Turbulent stratified flows are ubiquitous in nature, most notably in the Earth atmosphere or in oceans, but are highly challenging to study in laboratories. This impediment is due to the requirement of very large installations to monitor the different characteristic scales of turbulence. It is then of interest to construct idealized hydrodynamical models to more easily capture the transition towards disordered motions and explore connections with the spontaneous formation of density layers in stratified fluids (Oglethorpe *et al.* 2013). Indeed, the challenge of clearly explaining the layering and mixing, naturally present in geophysical flows, remains nowadays still open (see, e.g., Caulfield (2021) for a recent review). This question has fundamental ramifications as it directly relates to the transport of heat, pollutants or bio-mass in the density-stratified fluids present on Earth. Over the past decades, several contributions to the study of turbulent stratified flows have been made, seeking for a complete description of the mechanisms responsible for layering and mixing (Taylor *et al.* 2016; Zhou *et al.* 2017*a*,*b*). These works notably demonstrated that stratified turbulence inherits a strong anisotropy while developing and that inhomogeneous diffusive processes, such as mixing, are a direct consequence of this intermittent phenomenon.

† Email address for correspondence: joris.LABARBE@univ-amu.fr

The novelty of our approach lies in the generation of turbulence through instabilities of a model flow, namely the vertically-stratified horizontal plane Poiseuille flow (Le Gal *et al.* 2021). It is noteworthy to emphasize the difference with the more classical bi-dimensional case, where both stratification and shear lie on the same plane (Gage & Reid 1968). In fact, it is known since the studies of Basovich & Tsimring (1984) and Bakas & Farrell (2009*a*,*b*) that most environmental flows spontaneously generate internal gravity waves, whenever the stratification is oriented perpendicularly to the direction of motion. In addition, these small-scale waves propagate (with a Doppler-shift) and interact within the density layers, leading to the onset of instabilities (Satomura 1981). Historically, wave resonances in parallel sheared fluids have been introduced in the seminal paper of Cairns (1979) and further extended to diverse configurations of stratified flows (see, for instance, the review by Carpenter *et al.* (2011) on this topic). Moreover, such instabilities can transit to turbulence due to the collapse of finite disturbances, once the system saturates and reaches the nonlinear regime (Caulfield 1994). One benefit in considering instabilities is therefore the unnecessary need to trigger turbulence by explicit forcing, since the dynamics is self-sustained by definition. Hence, our study makes use of these instabilities to follow the route towards stratified turbulence, as done in a plethora of recent investigations on linear instabilities of stratified flows. We notably rely on the observations made for Taylor–Couette flows (Molemaker *et al.* 2001; Le Bars & Le Gal 2007; Le Dizès & Riedinger 2010; Park & Billant 2013), plane Couette flows with spanwise stratification (Facchini *et al.* 2018; Lucas *et al.* 2019), and a selection of rotating flows (Billant & Chomaz 2000; Le Dizès & Billant 2009; Riedinger *et al.* 2011). All the latter instabilities are indeed caused by the resonant interaction of Doppler-shifted internal gravity waves, which is the case in our context as well (Le Gal *et al.* 2021).

In this article, we demonstrate the presence of a symmetry-breaking mechanism, when the primary linear instability saturates and the flow enters the nonlinear regime. This modification in the streamwise mean velocity profile is a direct consequence of the interaction of linear harmonics, originally generated by counter-propagating internal gravity waves. The loss of invariance along the vertical additionally results in the formation of a localized region where the velocity fluctuates, inducing new spanwise shear in the system. As the gradients are sharpened, the flow eventually becomes subject to secondary instabilities that further saturate and break down into turbulence, through a series of bursting events (Lucas *et al.* 2017). We describe these spatially localized layers of turbulence by means of direct numerical simulations (DNS) in a doubly-periodic geometry with finite extension in the wall-normal direction. We support our observations with the computation of local measures of vertical shear and a series of averaged turbulent spectra to highlight this novel phenomenology.

The paper is structured as follows. Section 2 introduces the mathematical settings. Section 3 presents the linear stability analysis of our configuration and how the stability of discrete harmonics is determined accordingly. Section 4 is dedicated to DNS close to the instability threshold. We further discuss on the symmetry-breaking mechanism and the mean-flow interaction it induces. Section 5 describes the phenomenology observed when departing away from the onset of instability. We observe here the triggering of stratified turbulence, initiated from the mechanisms reported previously. Finally, we conclude our study in section 6 with some discussions and future extensions of this work.

2. Mathematical formulation

The present work deals with a model of incompressible linearly stratified shear flow enclosed between two parallel walls a distance D apart (Le Gal *et al.* 2021). This stratification is assumed to be directed along the orthogonal axis to that of the shear plane. The geometry considered here is the Cartesian frame of reference $(\boldsymbol{e}_X, \boldsymbol{e}_Y, \boldsymbol{e}_Z)$, with corresponding coordinates $\boldsymbol{X} = (X, Y, Z)$, describing the streamwise, cross-stream and vertical directions, respectively. Boundary conditions are no-slip and insulating on both walls. In addition, we assume periodicity along the other directions.

We consider a total density ρ departing linearly, along the Z-direction, from an otherwise constant density profile ρ_0. Under Boussinesq approximation, i.e. in the limit of $|\rho - \rho_0| \ll \rho_0$, we express this buoyancy field as

$$\rho(\boldsymbol{X}, T) = \rho_L(Z) + \rho'(\boldsymbol{X}, T), \tag{2.1}$$

where ρ' represents the fluctuating contribution and T is the dimensional time. Since we assume a stable stratification, the linear profile in (2.1) is written as $\rho_L(Z) = \rho_0(1 - ZN^2/g)$, where N is the Brunt-Väisälä frequency $N = \sqrt{-(g/\rho_0)(\mathrm{d}\rho_L/\mathrm{d}Z)}$ (assumed to be real and constant) and g is the constant acceleration due to gravity.

We render this configuration non-dimensional by means of an advective time scale $\tau = L/U$, with U being a local maximum of the mean velocity and $L = D/2$ a fixed measure of length. Coordinates are scaled accordingly, whereas pressure p and buoyancy b are expressed in the units of $\rho_0 U^2$ and $(\rho_0 N^2)/(gL)$, respectively. Hence, the non-dimensional velocity field $\boldsymbol{u} = (u, v, w)$, pressure p and buoyancy b are governed by the following set of equations

$$\partial_t \boldsymbol{u} + (\boldsymbol{u} \cdot \boldsymbol{\nabla})\, \boldsymbol{u} = -\boldsymbol{\nabla} p - Fr^{-2} b \boldsymbol{e}_z + Re^{-1} \nabla^2 \boldsymbol{u} + f \boldsymbol{e}_x, \tag{2.2a}$$

$$\partial_t b + (\boldsymbol{u} \cdot \boldsymbol{\nabla})\, b = w + (ReSc)^{-1} \nabla^2 b, \tag{2.2b}$$

$$\boldsymbol{\nabla} \cdot \boldsymbol{u} = 0, \tag{2.2c}$$

where f is a spatially uniform term enforcing the streamwise shear profile. This force can either correspond to a steady pressure gradient $f = -2Re^{-1}$ or an unsteady function ensuring conservation of the total mass flux $Q = \int_{-1}^{1} \int_{-L_x/2}^{L_x/2} u \mathrm{d}x \mathrm{d}y$. In both cases, and in the absence of instabilities, the balance between this external force and viscosity leads to the same base state velocity profile, the well-known plane Poiseuille solution $U_0(y) = 1 - y^2$, that is invariant in the z-coordinate. However, if the base system is unstable, we expect the choice of forcing to influence the nonlinear regime in some sort. We emphasize that equations (2.2) contain the Reynolds, Froude and Schmidt numbers as control parameters, defined by

$$Re = \frac{UL}{\nu}, \quad Fr = \frac{U}{LN}, \quad Sc = \frac{\nu}{\kappa}, \tag{2.3}$$

where ν and κ are the constant kinematic viscosity and diffusivity, respectively.

In the course of this study, we perform DNS of (2.2) by means of the spectral elements solver Nek5000 (Fischer 1997; Fischer *et al.* 2007). Our numerical domain consists in a rectangular parallelepiped of fixed size $\mathcal{D} = [-L_x/2, L_x/2] \times [-1, 1] \times [-L_z/2, L_z/2]$, designed such that the most unstable linear mode can develop. In addition, we assume periodic conditions and equispaced elements in both (x, z)-directions. On the contrary, we used a non-uniform distribution of wall-normal elements to refine the mesh closer to the walls. Computations were done using 10 elements per unstable streamwise wavelengths, 16 to 24 elements in the cross-stream direction and 18 to 24 elements along the vertical for a total of $\sim$ 13000 to 15000 elements, with a spectral order $N_s \in [8, 12]$ (number of

Gauss-Lobatto collocations points) and fixed values of $Sc = 1$ and $Fr = 2$. Numerical convergence of the results was checked by increasing the spectral order N_s. Following Le Gal *et al.* (2021), the flow is initiated from the parabolic Poiseuille profile plus some random infinitesimal perturbations on the buoyancy field (to double-check). Since we did not observed noticeable changes in the dynamics of the flow by using a constant pressure gradient or a constant flux, we therefore focused our attention on the latter to better fit with the experimental conditions described in Le Gal *et al.* (2021).

3. Linear stability analysis

3.1. *Global stability analysis*

We perform a linear stability analysis of equations (2.2) by means of a pseudo-spectral collocation method. Perturbations of the basic state are expressed in terms of normal modes, taking advantage of the periodicity of the flow. Therefore, we introduce spatial wavenumbers (k_x, k_z) (assumed to be real), as well as the complex frequency ω, to expand perturbations $\boldsymbol{q}' = (\boldsymbol{u}', p', b')$ as

$$\boldsymbol{q}'(\boldsymbol{x}, t) = \hat{\boldsymbol{q}}(y) \exp\left[\mathrm{i}(k_x x + k_z z - \omega t)\right] + \text{c.c.}, \tag{3.1}$$

where c.c. stands for 'complex conjugate'.

Substituting (3.1) within (2.2), while taking the divergence of (2.2a), we recover a differential expression for the pressure eigenfunction. The latter allows us to express the stratified Orr-Sommerfeld equation, for the cross-stream velocity perturbation $\hat{v}$. Subsequently, we recover the Squire equation, governing the perturbation of axial vorticity $\hat{\eta}$, by applying the curl operator on the wall-normal projection of (2.2a). The resulting linear system yields

$$\left[k_x\left(U_0\widehat{\nabla}^2 - \mathrm{d}^2U_0/\mathrm{d}y^2\right) + \mathrm{i}Re^{-1}\widehat{\nabla}^4\right]\hat{v} - Fr^{-2}k_z\mathrm{d}\hat{b}/\mathrm{d}y = \omega\widehat{\nabla}^2\hat{v}, \tag{3.2a}$$

$$k_z\left(\mathrm{d}U_0/\mathrm{d}y\right)\hat{v} + \left(k_xU_0 + \mathrm{i}Re^{-1}\widehat{\nabla}^2\right)\hat{\eta} - Fr^{-2}k_x\hat{b} = \omega\hat{\eta}, \tag{3.2b}$$

$$-k^{-2}\left(k_z\mathrm{d}\hat{v}/\mathrm{d}y + k_x\hat{\eta}\right) + \left[k_xU_0 + \mathrm{i}\left(ReSc\right)^{-1}\widehat{\nabla}^2\right]\hat{b} = \omega\hat{b}, \tag{3.2c}$$

where $k^2 = k_x^2 + k_z^2$ is the wavevector squared norm and $\widehat{\nabla}^2 = \mathrm{d}^2/\mathrm{d}y^2 - k^2$ is the Laplacian operator in Fourier space. System (3.2) describes a boundary eigenvalue problem of the form $A\hat{\boldsymbol{\xi}} = \omega B\hat{\boldsymbol{\xi}}$, for the eigenfrequency ω and eigenfunction $\hat{\boldsymbol{\xi}} = [\hat{v}, \hat{\eta}, \hat{b}]^T$ (the overscript denotes transposition). The latter set of equations is supplemented with no-slip and insulating boundary conditions, reading $\hat{v} = \mathrm{d}\hat{v}/\mathrm{d}y = \hat{\eta} = \mathrm{d}\hat{b}/\mathrm{d}y = 0$ at $y = \pm 1$.

We use a Galerkin approach to discretize the differential operators, based on the expansion of the eigenfunctions in terms of Chebyshev polynomials. Simultaneously, we apply a collocation method at the Gauss–Lobatto quadrature nodes

$$y_j = \cos\left(\frac{j\pi}{M+1}\right), \quad j = 1, \ldots, M\,, \tag{3.3}$$

for a fixed truncation order M. We verified the convergence of this method, based on the relative error of the eigenvalues of (3.2), as M was increased. In general, a value of $M \sim 40$ was large enough to reach a reasonable tolerance.

3.2. *Results*

The classical unstratified ($Fr \to +\infty$) plane Poiseuille flow is subject to a linear instability, due to the growth of a Tollmien–Schlichting (TS) wave (Tollmien 1929;

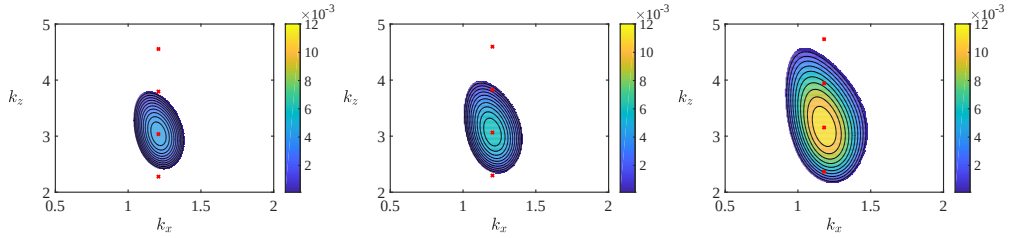

(a) $Re = 550$ (b) $Re = 580$ (c) $Re = 700$

Figure 1: Growth rate contours in the (k_x, k_z)-space from the linear stability analysis of equations (3.2) at $Fr = 2$, $Sc = 1$ and over different Reynolds numbers. Red crosses correspond to the discretized modes present in our DNS domain (cf. section 4). White regions correspond to negative growth rates, i.e., stability.

Schlichting 1933). This well-known instability occurs at a critical Reynolds number $Re_c \sim 5770$ (Orszag 1971) and has been extensively studied to examine the transition from laminar flows to turbulence. As shown in (Le Gal *et al.* 2021), the consideration of a vertical profile of stable stratification greatly lowers the instability threshold. The principal argument suggested by the authors is that such a flow allows for resonances of internal gravity waves (among themselves or eventually with viscous TS waves), leading to the onset of a new instability. A similar conclusion was drawn in the context of plane Couette flow, where a growth of perturbations due to the resonance of Doppler-shifted gravity waves was observed (Facchini *et al.* 2018). We recall though that Couette flow is unconditionally stable to infinitesimal disturbances in the unstratified limit and maintained by viscosity, which is not the case here.

Our interest for the present article is to go beyond the results obtained in Le Gal *et al.* (2021), by conducting a thorough analysis of the nonlinear saturation of this recently discovered instability. Therefore, we make profit of the linear stability results to extract the optimal wavenumbers $(k_x^{\mathrm{opt}}, k_z^{\mathrm{opt}})$, associated with modes of largest growth rates for a given set of control parameters. We display in figure 1 the stability results at different Reynolds numbers, close to the instability threshold (for this set of parameters, we have $Re_c \sim 480$). We recall that $Fr = 2$ and $Sc = 1$ (differing thus from experimental values). The red crosses in this figure represent the location in the wavenumber space of the discretized modes present in our DNS domain, see section 4 below. We then determine whether unstable harmonics of the fundamental mode are present within the unstable region or not. It becomes clear that the case $Re = 550$ contains only stable harmonics, whereas the other two cases allow unstable harmonics within the domain of instability.

4. Weakly nonlinear saturation near the onset

As already mentioned, the numerical domain chosen is an elongated rectangular parallelepiped of size $\mathcal{D} = [-\lambda_x/2, \lambda_x/2] \times [-1, 1] \times [-2\lambda_z, 2\lambda_z]$, with fundamental wavelengths $\lambda_x = 2\pi/k_x^{\mathrm{opt}}$ and $\lambda_z = 2\pi/k_z^{\mathrm{opt}}$ which depend on the control parameters. Our main focus being the possible emergence of modulation along the z-coordinate, this is why we consider boxes encompassing multiple unstable wavelengths along the vertical. However, we do not explore possible horizontal modulation since we restrict the streamwise extension to only one unstable wavelength. We monitor the growth of

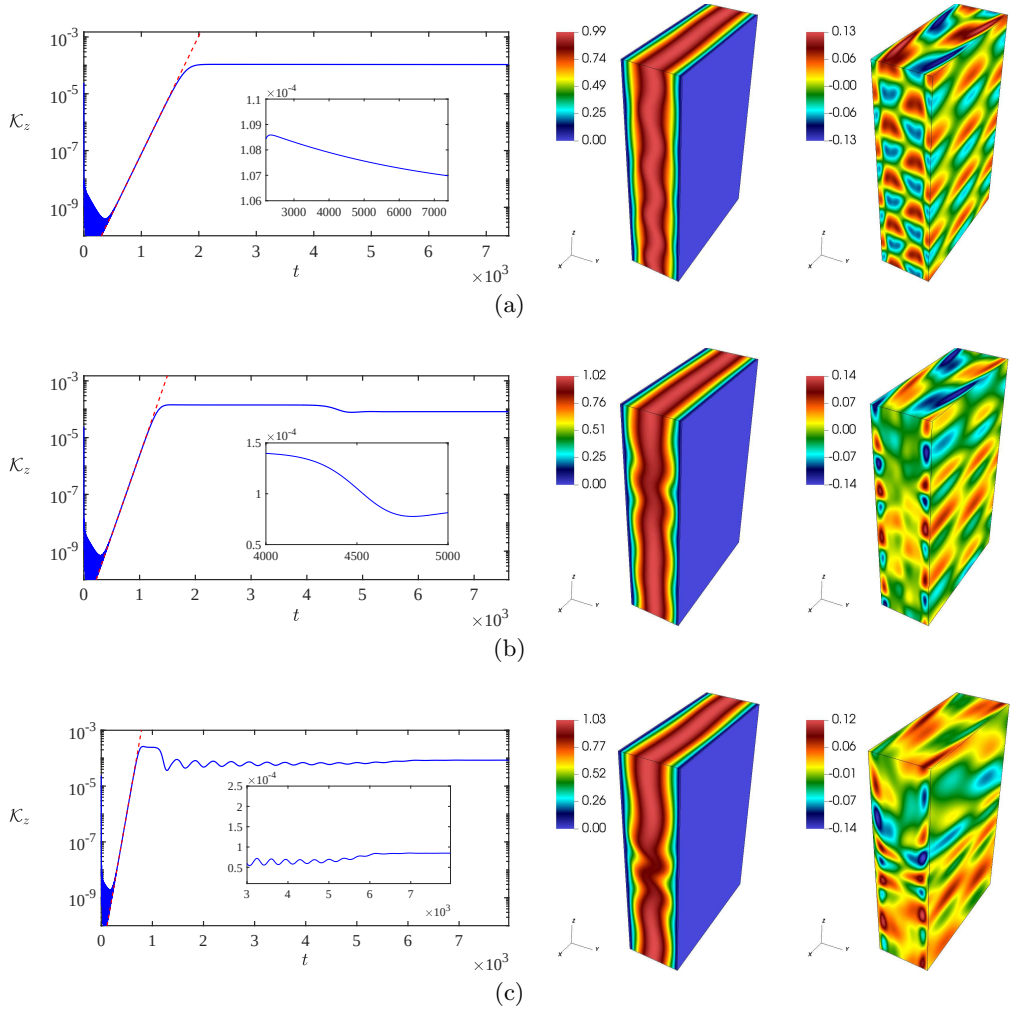

Figure 2: Vertical kinetic energy curves (in logarithmic scale) over time, with snapshots of the streamwise velocity and buoyancy perturbation, computed at the latest time of the simulations. Values of Reynolds numbers correspond to, respectively, (a) $Re = 550$, (b) $Re = 580$ and (c) $Re = 700$. Red dashed lines in left panels represent twice the growth rates of the dominant unstable mode, as predicted from linear theory. Close-up views are displayed for each configuration, highlighting the nonlinear behaviour.

instability by computing the quantity

$$\mathcal{K}_z = \frac{1}{2}\langle w^2 \rangle_{\mathcal{D}} = \frac{1}{2\mathcal{D}} \int_{\mathcal{D}} w^2 \mathrm{d}V, \tag{4.1}$$

where $\langle \cdot \rangle_{\mathcal{D}}$ denotes averaging over the volume $\mathcal{D}$. We therefore expect, from the definition of (4.1) and linear theory, to first observe an exponential increase in energy, following a slope of twice the growth rate.

We start by presenting in figure 2 a set of vertical kinetic energies, computed over time, for Reynolds numbers close to the instability threshold (in the present case, $Re_c \sim 480$). In addition, we add snapshots of the streamwise velocity and perturbed buoyancy profile

at the latest instant of computation (last point of the energy curves). Not surprisingly, we notice the exponential growth of disturbances in the first part of each curve. The slope in logarithm scale is further confirmed from linear stability analysis, as shown by the red dashed lines. Then, once the perturbations reach an order of magnitude similar to that of the base flow, nonlinearities are no longer negligible and the system departs from linear theory.

The first case of interest, $Re = 550$, is fairly simple to understand as the instability saturates in the form of a quasi-stationary solution (we still nevertheless observe a small decay over a viscous time in the nonlinear regime as shown by the insert in figure 2a). The saturated amplitude represented here corresponds physically to a meandering in the streamwise velocity, according to the velocity snapshot displayed in the same figure. Similar profiles have already been observed in the experiment of Le Gal *et al.* (2021). Besides this steady and vertically homogeneous configuration, we notice interesting features in the other two panels, corresponding to the computations at $Re = 580$ and $Re = 700$. There is indeed a finite time at which this homogeneous state departs from the primary branch via a point of secondary bifurcation, as displayed in the inserts of figure 2. Once the bifurcated solutions reach a stationary state, at the end of each simulations, the corresponding velocity and buoyancy profiles are no longer homogeneous. As a consequence, a localized structure of velocity emerges along the vertical and the the buoyancy perturbations also become inhomogeneous and localized. Clearly, we observe a spontaneous pattern formation due to a symmetry-breaking mechanism, our system being initially invariant along z.

Since we notice in most of the cases a loss of symmetry along the vertical, it is therefore of great interest to introduce an averaging operator for quantifying horizontal measures, defined as $\langle\cdot\rangle_H \coloneqq (2\lambda_x)^{-1}\iint\cdot\,\mathrm{d}x\mathrm{d}y$. One way to capture and identify the peculiar transition described earlier is to compute Hovmöller diagrams of the horizontally-averaged streamwise velocity fluctuation $\langle u - U_0\rangle_H$. This is represented in figure 3 for the three configurations we are interested in. As we already noticed earlier, the case corresponding to $Re = 550$ displays harmonic modulation of the horizontally-averaged streamwise velocity which is slowly drifting in time. Note that this is effectively a correction to the initially z-invariant Poiseuille profile, although it remains small in amplitude at this Reynolds number. We expect this modulation to be suppressed as the simulation reach a large enough viscous time (scaling thus with Re) and a stationary solution would ultimately be restored. The characteristic shift observed here essentially depends on the initial random seed used for the computation. We observed different drifts depending on the initial conditions (not shown). Pursuing our investigation, the most striking observation from figure 3b is the sudden coarsening of the mean flow modulation, at the finite time corresponding to the secondary bifurcation in figure 2b. The system indeed undergoes for $t \sim 4 \times 10^3$ a symmetry-breaking mechanism, allowing for the formation of a box-scale modulation of the mean Poiseuille profile that is not harmonic: the region of reduced streamwise velocity is sharp and localized while the accelerated region is broader (see figure 4 below). We recall that the streamwise mass flux is conserved in all of our simulations. It is worth noticing that this phenomenon fills the whole numerical domain and saturates in the form of a steady nonlinear solution. More surprisingly, the case of $Re = 700$ displayed in figure 3c also depicts the same symmetry-breaking mechanism (although at a shorter time), with a localized structure in the velocity profile, but converges instead to a drifting mode. This uniform shift seems to not be related with the drift observed at $Re = 550$, since we observe it irrespective of the initial conditions, and most certainly requires a nonlinear analysis to determine its origin. This task is left for a future work on the subject, as it goes beyond the scope

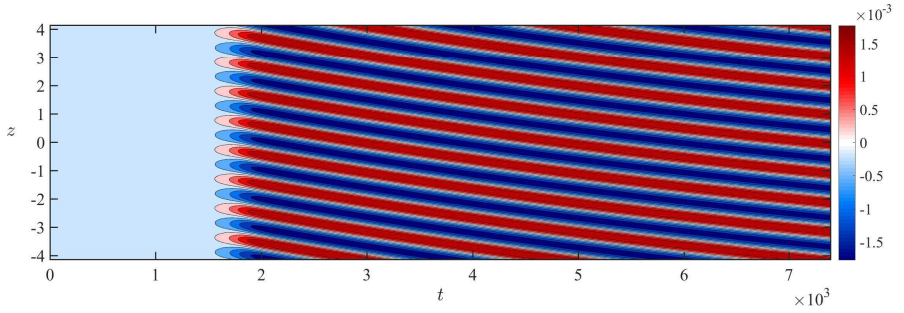

(a) $Re = 550$

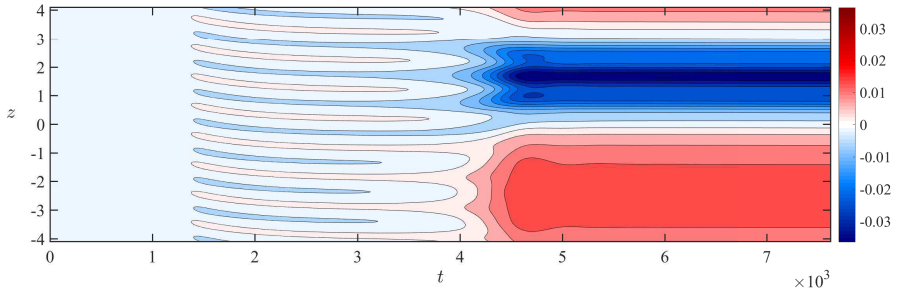

(b) $Re = 580$

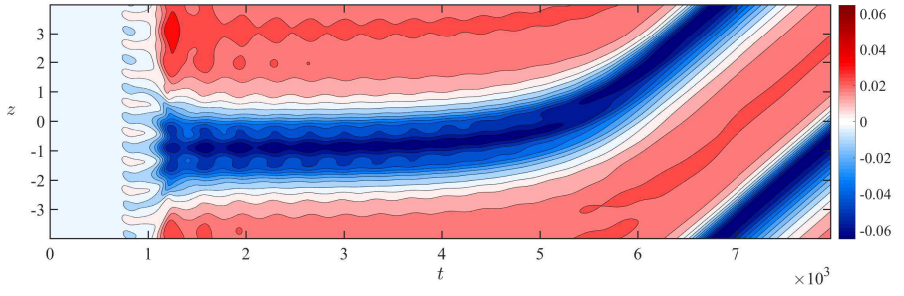

(c) $Re = 700$

Figure 3: Hovmöller diagrams of the horizontally averaged streamwise velocity fluctuation $\langle u - U_0 \rangle_H$, computed in (t, z)-plane. Positive (negative) values are displayed in red (blue). The areas of constant color on the left of each panels represent the exponential growth of disturbances.

of this article. We recall here that a very similar phenomenology is observed when using the more classical imposed pressure gradient forcing to sustain the mean Poiseuille flow. It is naturally emerging from the nonlinear interaction of unstable waves with the mean flow, regardless of the force sustaining it.

Let us now investigate the wave-mean flow interaction that is depicted here, using arguments from linear theory. Making profit of the averaging operator over the horizontal plane introduced earlier, we define the Reynolds-averaged decomposition of the field $\boldsymbol{q} = (\boldsymbol{u}, p, b)$, as

$$\boldsymbol{q} = \langle \boldsymbol{q} \rangle_H(z, t) + \boldsymbol{q}'(x, y, z, t), \tag{4.2}$$

separating thus the horizontal mean flow from the fluctuations. Substituting (4.2) in the

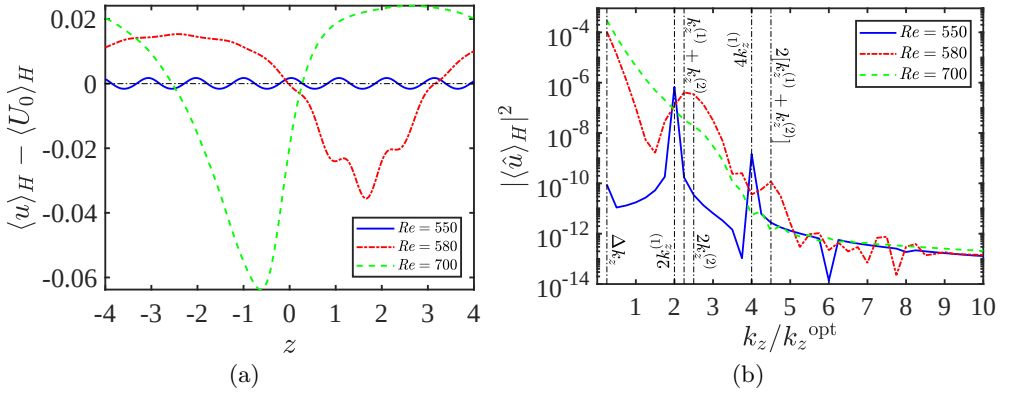

Figure 4: Each curve is computed at the latest time of simulation in figure 3, once the solution has converged. (a) Horizontally-averaged streamwise velocity fluctuations as a function of the vertical coordinate. (b) Spectral energy in Fourier space of the averaged velocity profiles from the left panel. The principal amplitude peaks are displayed with vertical lines and captioned with their associated representation defined in expression 4.5.

streamwise projection of equation (2.2a), along with boundary conditions, we recover the mean field equation

$$\frac{\partial}{\partial t}\langle u \rangle_H + \frac{\partial}{\partial z}\langle u'w' \rangle_H = Re^{-1}\left(\frac{\partial^2}{\partial z^2}\langle u \rangle_H + \langle \frac{\partial^2 u}{\partial y^2} \rangle_H\right) + \langle f \rangle_H. \tag{4.3}$$

Equation (4.3) expresses the evolution of the mean flow and the transfer of momentum, by means of the divergence of Reynolds stresses (the second term in the left-hand side). If we consider the fluctuations to be written as a superposition of both upward and downward modes with distinct but close wavenumbers $(k_z^{(1)}, k_z^{(2)})$ and frequencies $(\omega^{(1)}, \omega^{(2)})$, we obtain

$$\begin{aligned} u' = {} & \hat{u}_{11} e^{\mathrm{i}(k_x x + k_z^{(1)} z - \omega^{(1)} t)} + \text{c.c.} + \hat{u}_{12} e^{\mathrm{i}(k_x x - k_z^{(1)} z - \omega^{(1)} t)} + \text{c.c.} \\ & + \hat{u}_{21} e^{\mathrm{i}(k_x x + k_z^{(2)} z - \omega^{(2)} t)} + \text{c.c.} + \hat{u}_{22} e^{\mathrm{i}(k_x x - k_z^{(2)} z - \omega^{(2)} t)} + \text{c.c.}, \end{aligned} \tag{4.4}$$

with the same decomposition holding for w'. Subsequently, we expand the Reynolds stress term in (4.3), using the modal decomposition (4.4), and we find

$$\begin{aligned} \langle u'w' \rangle_H = {} & \langle \hat{u}_{11}\hat{w}_{11}^* + \hat{u}_{12}\hat{w}_{12}^* + \hat{u}_{21}\hat{w}_{21}^* + \hat{u}_{22}\hat{w}_{22}^* \rangle_H + \text{c.c.} \\ & + \langle \hat{u}_{11}\hat{w}_{12}^* + \hat{u}_{12}^*\hat{w}_{11} \rangle_H e^{2\mathrm{i}k_z^{(1)} z} + \text{c.c.} + \langle \hat{u}_{21}\hat{w}_{22}^* + \hat{u}_{22}^*\hat{w}_{21} \rangle_H e^{2\mathrm{i}k_z^{(2)} z} + \text{c.c.} \\ & + \langle \hat{u}_{11}\hat{w}_{22}^* + \hat{u}_{22}^*\hat{w}_{11} \rangle_H e^{\mathrm{i}[(k_z^{(1)} + k_z^{(2)})z - \Delta\omega t]} + \text{c.c.} \\ & + \langle \hat{u}_{11}\hat{w}_{21}^* + \hat{u}_{21}^*\hat{w}_{11} \rangle_H e^{\mathrm{i}(\Delta k_z z - \Delta\omega t)} + \text{c.c.}, \end{aligned} \tag{4.5}$$

where the overscript denotes complex transposition and for $\Delta k_z = k_z^{(1)} - k_z^{(2)}$ and $\Delta\omega = \omega^{(1)} - \omega^{(2)}$ (a similar description with only one pair of modes can be found in Yang *et al.* (2022)). We distinguish in (4.5) the contributions from self- and cross-interactions between a fixed set of discretized modes. As one can notice, computing the vertical divergence of the whole expression removes the contribution of self-interacting modes (the first term in the right-hand side) from the mean flow equation. However,

cross-interaction of modes with the same vertical structure (second and third terms of the expression) yields a wave pattern with twice the original wavenumber.

We represent in figure 4 snapshots of the averaged velocity fluctuations $\langle u - U_0 \rangle_H$ (we recall that $U_0 = 1 - y^2$ is the plane Poiseuille profile), at the latest time of computations for each panel in figure 3. Clearly, we notice the loss of homogeneity, originally present in the solution at $Re = 550$, when observing the other two curves. For instance, the transient solution $Re = 580$ still displays the wave pattern at twice the initial wavenumber from the later case, but also tends to form a modulation filling the numerical box. Additionally, we explore the spectral energy of the converged solution at, first, $Re = 550$ in figure 4b and notice, as expected, the two peaks at $2k_z^{\mathrm{opt}}$ and its harmonics (with the correspondence $k_z^{\mathrm{opt}} = k_z^{(1)}$ from expression (4.5)). We can easily notice this pattern to emerge in the non-linear regime of the first simulation at $Re = 550$, as displayed in figures 3a and 4a, with a total wavenumber of $8k_z^{\mathrm{opt}}$ (since the domain originally contains 4 unstable wavelengths). This same spatial structure is also present in the early stages of figures 3b and 3c, until the time where the other modes start to contribute to the dynamics and break the symmetry. The intermediate case, $Re = 580$, shows a transient solution with a leading mode of wavenumber $\Delta k_z = k_z^{\mathrm{opt}}/4$ present in the spectrum of figure 4b. Moreover, there exists lower peaks corresponding to $k_z^{(1)} + k_z^{(2)} = 9k_z^{\mathrm{opt}}/4$, $2k_z^{(2)} = 5k_z^{\mathrm{opt}}/2$, with their harmonics, but they all are dominated by the mode at the size of the whole domain. Finally, the spectrum of the latest configuration at $Re = 700$ is completely dominated by the mode of wavenumber Δk_z and enclosed by two sharp fronts of velocity. This profile is represented in figure 4a and highlight the generation and amplification of vertical shear, due to the increasing velocity gradient in that direction (with an order of magnitude of ~ 1 to 10%). We conclude that this spontaneous large-scale modulation is thus mainly due to an interaction of closely spaced unstable harmonics, generating interesting space-time wave patterns. Not surprisingly, these symmetry-breaking secondary bifurcations happen at a shorter time as the control parameter (Re) increases, allowing indeed more harmonics within the instability map. A demonstration of this feature was represented using linear theory in figure 1, with red crosses depicting the different harmonics.

We now try exploring configurations away from the instability threshold, to investigate whether we still observe a similar phenomenology and how it transits to turbulence.

5. Localized stratified turbulence far from the onset

Departing away from the instability threshold, we expect the flow to behave in a more chaotic way and we notably seek for the trigger of stratified turbulence. As already noticed in a previous study on the plane Couette profile with spanwise stratification (Lucas *et al.* 2019), the onset of turbulence occurs at large Re in regions with largest vertical velocity gradients. It appears that the mechanism responsible for these events is induced by a secondary instability, of Kelvin–Helmholtz (KH) type (Miles 1961; Howard 1961), allowing for the development of overturning. We therefore pay great attention in our computations on the local quantities determining the tendency of the flow to be subject to secondary shear instabilities. In particular, we establish local expressions for the Froude and gradient Richardson numbers (Lucas *et al.* 2017), as follows

$$Fr_z = \frac{Fr}{\sqrt{1 - Fr^2 \langle \partial_z b \rangle_H}}, \quad Ri_z = \frac{1}{Fr_z^2 \langle \partial_z u \rangle_H^2}. \tag{5.1}$$

It is worth emphasizing that our system is initially homogeneous in the vertical direction, such that $Fr_z|_{t=0} = Fr$ and $Ri_z|_{t=0} = \infty$.

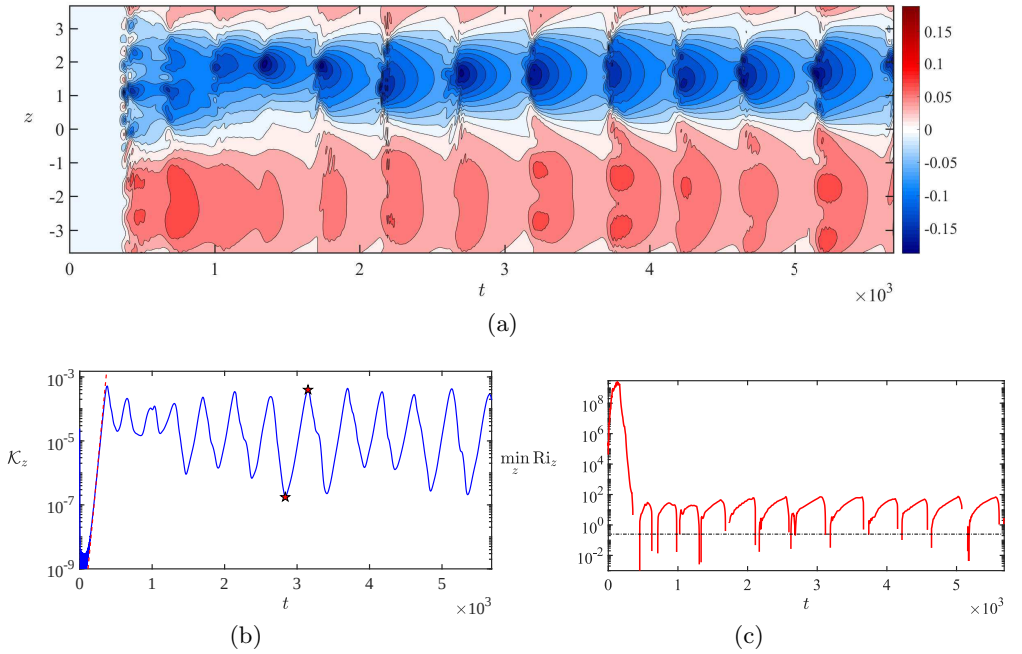

Figure 5: DNS at $Re = 1500$. (a) Hovmöller map of streamwise mean velocity fluctuations, with the same color code as in figure 3. (b) Vertical kinetic energy in the spirit of figure 2. The two red markers indicate the extrema of a bursting episode, computed in details in figure 6. (c) Vertical minimum of gradient Richardson number over time, computed in logarithmic scale. The curve is discontinuous whenever Ri_z is complex-valued (when the flow becomes locally unstable to convection). The thin dashed-dotted line delimits the KH instability threshold of $Ri_z = 1/4$ (Miles 1961; Howard 1961).

We represent the local Richardson number in figure 5, along with the vertical kinetic energy and the Hovmöller diagram for the case $Re = 1500$, highlighting the saturation of the linear Poiseuille instability and the appearance of a non-trivial dynamics. First, we still observe the large-scale vertical modulation of the mean Poiseuille profile discussed in the previous section. This phenomenon is therefore robust and persists well beyond the weakly nonlinear regime. Second, we observe in all the panels a series of bursting episodes, consisting in cycles of energy growths and decays. Soon after the symmetry-breaking transition at $t \sim 300$, the local Richardson number in figure 5c drastically falls until reaching a small interval of time where it becomes complex-valued. This peculiarity emphasizes the presence of convection (stratification becomes unstable) locally and supports the onset of a secondary shear instability. We study further the quasi-periodic patterns displayed over time in figures 5b and 5c, and explain this series of events as a consequence of the loss of vertical homogeneity, leading to the growth of vertical shear. Indeed, once the Richardson number becomes low enough to cross the theoretical threshold of $Ri_z = 1/4$ (Miles 1961; Howard 1961), the flow strengthens due to this secondary instability, until saturation, and then collapses into unsteady motion. Afterwards, energy diminishes due turbulent dissipation and presumably because the secondary instability has disappeared due to a mixing event, or the reduction in vertical shear. The mean flow is then restored to a state dominated by the interaction of internal gravity waves. From a dynamical

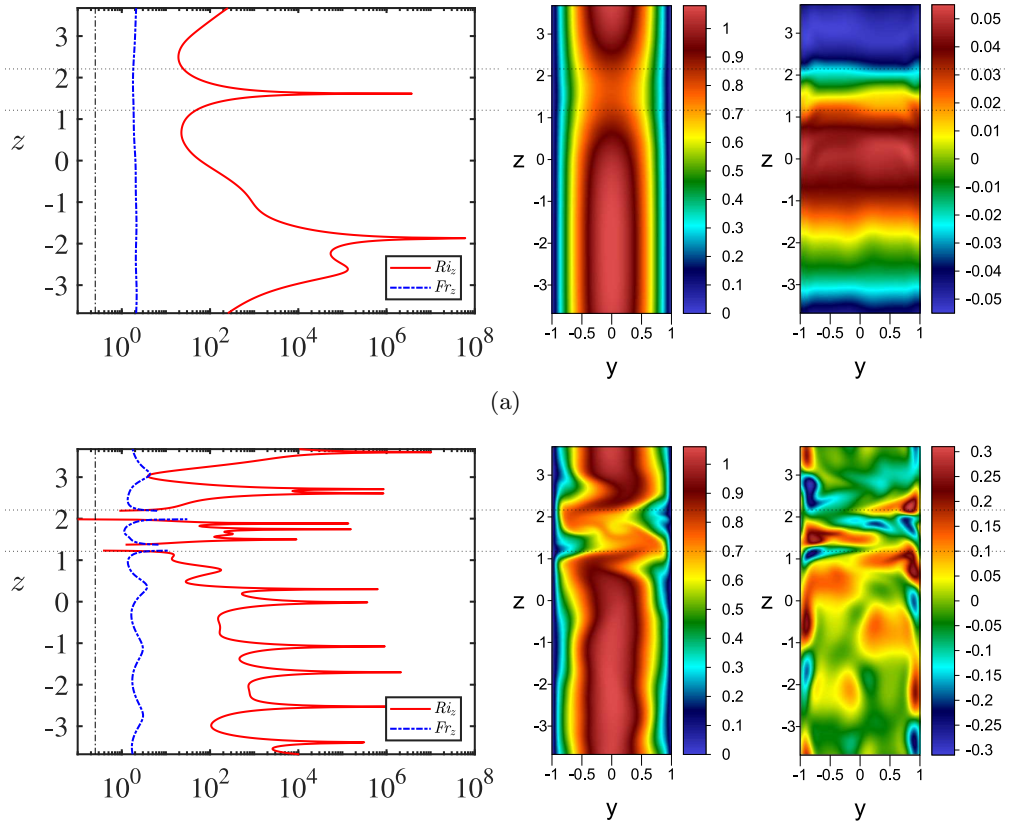

Figure 6: Local measures of Froude and Richardson numbers (in logarithmic units) over the vertical coordinate, for the case $Re = 1500$. Data and snapshots are computed at (a) $t = 2837$ and (b) $t = 3151$ (see figure 5). Second and third panels of each rows represent the streamwise velocity and the fluctuation of buoyancy at an arbitrary position along x, respectively. The upright straight line in the left panel indicates the threshold of KH instability. The thin dotted lines passing through each panel set delimit the interfaces where the secondary instabilities trigger and the flow collapses into stratified turbulence.

point of view, we can view the system as trapped in a quasi-periodic attractor. Similar observations were made in the context of forced stratified turbulence, in relation with the formation of density layers (Lucas *et al.* 2017).

A surprising feature of figure 5a we did not discussed, is the robustness in the local modification of the velocity profile. The region where the fluctuations decelerate the mean flow remains indeed located within a fixed interval along the vertical extension. As the energy increases, this thin layer shrinks further and hence, the velocity gradients strengthen. To have a clearer view, we present snapshots of velocity and buoyancy profiles in figure 6 at both extrema of a bursting episode (denoted by the stars in figure 5b). It is evident from the representation of density fluctuations in figure 6a that domains of quiescent flow, surrounding the area of lowest horizontal velocity, slightly enhance the stratification profile. The two layers encompassing this region are both subject to the strongest vertical shear and therefore, correspond to the lowest values of Ri_z in figure 6b. At the peak of energy, the stratification becomes unstable (with overturning) at these

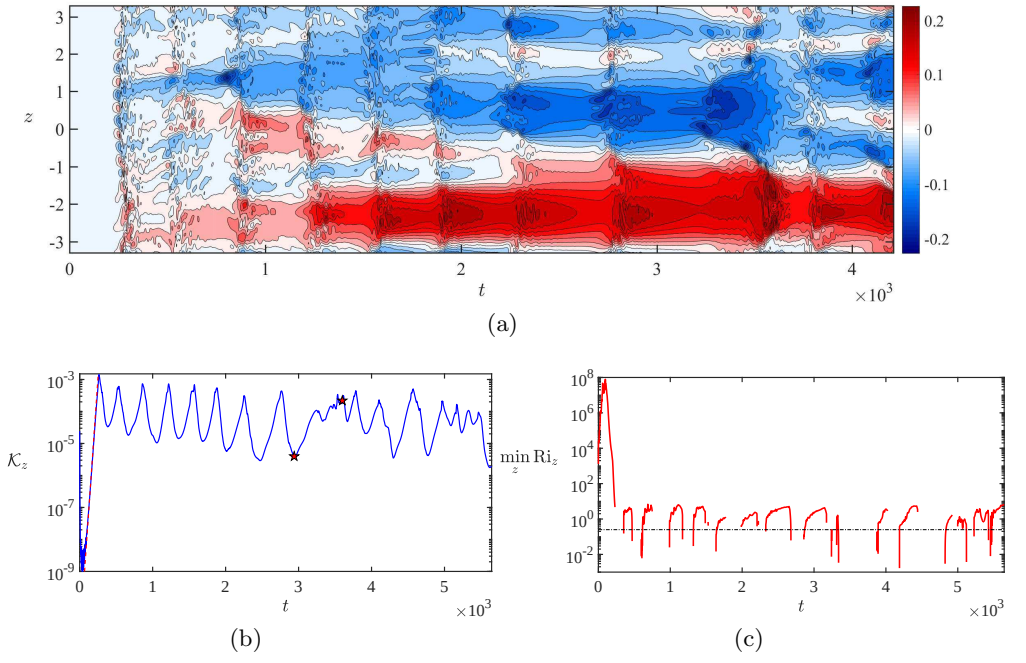

Figure 7: DNS at $Re = 5000$. Same panels as in figure 5. The red markers in the representation of vertical kinetic energy indicate the time coordinates used in the snapshots of figure 8.

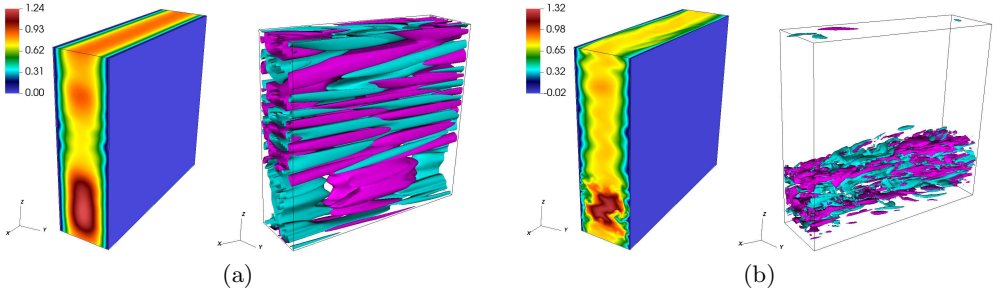

Figure 8: Snapshots of the numerical computation at $Re = 5000$, computed at (a) $t = 2940$ and (b) $t = 3600$. Left panels of each column display the streamwise velocity, whereas right panels represent the associated iso-contours of wall-normal velocity. Positive (negative) iso-contours are represented in light purple (light blue) regardless of their magnitude.

coordinates and the flow breaks down into a localized layer of chaotic motions. Strikingly, these disordered motion remain confined within a fixed interval (delimited by the thin dotted lines), before returning back to the original layered configuration displayed in figure 6a. This back-and-forth dynamics is well depicted through the Hovmöller diagram in figure 5a.

Increasing further the Reynolds number up to $Re = 5000$, we present in figure 7 the same set of data than in figure 5. One instantaneous observation that one can make about the first panel is the complexity of the Hovmöller diagram in the large Re configuration.

The interfaces are indeed no longer formed in an organized way, as previously, but they follow instead a coarse-graining dynamics of intermittent patterns. Some regions of positive/negative velocity fluctuations occasionally emerge out of nowhere and then sustain or not thin layers of stratified turbulence, due to similar bursting events as previously. In the meantime, we still observe through the simulation a dominant mode slowly emerging, at the size of the domain. This lead us to think that the resonance of harmonics with the fundamental mode dominates the other interactions. Once again, the vertical kinetic energy displays a series of back-and-forth episodes while the local Richardson numbers are now almost always below the threshold of instability, or even imaginary. It is thus not surprising to notice additional regions of intermittency in the data, such as in figure 6b, as turbulent states now largely influence the global dynamics. As we did for the case of $Re = 1500$, we present in figure 8 several snapshots of horizontal velocity, taken at the times of lowest and largest energy peaks in a bursting episode. We distinctly notice one large region subject to shear instabilities, further collapsing into highly chaotic motions. Although the bursting events are now way more forceful than previously, the flow still relaminarises before starting over a new cycle. This dynamics seems to persist over the simulations and we expect the system to behave similarly as the vertical extension is modified, as soon as resonances are permitted within the numerical domain. To demonstrate this behaviour, we compute in both panels of figure 8 a visualization of the velocity field at $t = 2940$ first, where the flow is assumed to be mostly laminar, and then at $t = 3600$, where localized turbulence is observed. We highlight the evidence of such local turbulent events, as in the second panel of figure 9, by computing a set of turbulence spectra from the mean spectral energy of the streamwise velocity. The spectrum averaged over a full period and over the (y, z) spatial coordinates is depicted with a continuous blue line. Departing from such reference, we can split this spectrum between the contributions above and below a certain energy level, say $\mathcal{K}_z = 6 \times 10^{-5}$ in figure 7b. We represent the two spectra in dashed-dotted line within the same figure and notice a great difference among them. It is clear that low energy levels correspond to stable configurations of laminar flows with a steep spectrum, whereas the high energy portions contain the turbulent information. Alternatively, we can also separate the spectrum along the vertical direction, by solely computing spectra inside and outside the localized layers, whenever turbulence triggers. These two spectra are represented in dotted line and emphasize clearly the local character of our system. We further notice a tolerable agreement in these spatial regions with the classical $-5/3$ power law prediction (Lindborg 2006), although a definitive conclusion about spectral exponents would require much higher Reynolds number simulations. The reasons for the discrepancy with the classical power laws might be due to the buoyancy Reynolds being too small (Brethouwer *et al.* 2007) and because of the intermittent nature of our turbulent events. We still make use of these observations to support our discovery of the spontaneous formation of localized turbulent layers, arising from the instability of the vertically-stratified Poiseuille flow.

6. Discussion

Along this article, we have presented a series of results on the plane Poiseuille flow with stable vertical stratification. One of the main reasons we studied this configuration is, as it was originally done in the unstratified limit, to study the transition from a laminar flow, subject to a linear instability, towards the onset and development of turbulence. First, we found that this system loses its vertical homogeneity as a consequence of an interaction of modes, whenever the numerical domain is elongated enough to allow unstable harmonics

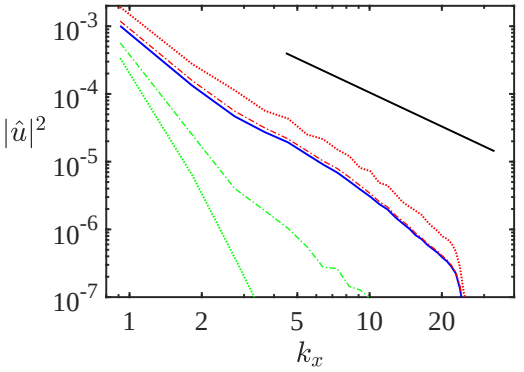

Figure 9: Streamwise kinetic energy spectrum in Fourier space for the case $Re = 5000$. The spectrum represented by the blue continuous line is averaged in space over the (y, z)-coordinates and in time over a characteristic period of a turbulent event. The spectrum in red (green) dashed-dotted line is averaged in space over the (y, z)-coordinates and for each interval of time above (below) a critical energy value of $\mathcal{K}_z = 6 \times 10^{-5}$ (cf. curve in figure 7b). The spectrum in red (green) dotted line is averaged in space over the y-coordinate and over the interval in z inside (outside) each turbulent layer at the finite times where turbulence triggers. The straight black line represents the classical $-5/3$ power law (Lindborg 2006) and is shown for reference.

of the fundamental mode to exist. The result of this symmetry-breaking mechanism is the spontaneous formation of vertical velocity gradients in the initially homogeneous Poiseuille profile. This additional shear induces secondary instabilities of KH type, as well as overturning events, confined in regions where the gradient Richardson number crosses the well-known critical threshold (Howard 1961; Miles 1961). Once this instability saturates and collapses into stratified turbulence, energy declines and the system returns to the state it formerly was in, before the onset of instability. This back-and-forth dynamics of bursting episodes, enclosed within finite layers, is a remarkable finding that, to the best of our knowledge, has never been observed (under this form) in the literature. However, it is not clear at this stage how the mean flow modulation will manifest itself in the limit of extremely elongated domain in the vertical direction, where a large number of unstable modes can coexist even close to the threshold. It also remains to verify whether such modulation can also occur in the streamwise direction if multiple horizontal wavelengths can fit into the numerical domain.

An important feature of this flow is, as mentioned, the spontaneous layering and the onset of turbulence, due to subsidiary shear instabilities. Moreover, these turbulent motions are encompassed between thin layers of finite size, delimited by interfaces where the Richardson number is the lowest. It is further observed that such regions are surrounded by a flow displaying the same meandering patterns as originally noticed by Le Gal *et al.* (2021). As the Reynolds number is increased, intermittency takes place and we are no longer able to distinguish an organized formation of turbulent layers. In this context, configurations with several set of layers (all undergoing a series of bursting events) are even allowed to exist. These observations tend to highlight the presence of a similar homoclinic snaking mechanism than some dynamical systems are subject to (Burke & Knobloch 2007). In recent articles, close connections between the field of pattern formation and the development of coherent structures, related to the layering of the flow, have been extensively studied (Lucas *et al.* 2017), notably in the context of

unstratified plane Couette flow (Schneider *et al.* 2010; Gibson & Schneider 2016). These works demonstrated the existence of invariant solutions, restricted to one spatial dimension, using Newton-like algorithms to perform a parameter continuation. Eventually, we could consider a similar treatment in our framework, although computation of vertically-localized solutions for such configuration is numerically expensive and requires therefore a better understanding of the weakly nonlinear dynamics.

To explain the symmetry loss in the nonlinear regime, we decomposed the disturbances as a superposition of linear modes, while setting ourselves in the vicinity of the instability threshold. This allowed us to extract an explicit form for the Reynolds stress, assuming the domain contains a finite number of harmonics. Although this approach is useful to understand the mechanism responsible for the onset of a secondary bifurcation and for the emergence of space-time modulations, it still adopts arguments from linear theory, which are no longer strictly valid in this regime. To avoid such impediment, a next step would be to investigate the weakly nonlinear analysis of the system, with finite amplitudes, shortly after the deviation from linear instability. With such a study, we would be able to isolate the term responsible for the correction of the mean flow and derive a set of nonlinear equations to describe its dynamics (in the form of a modified Stuart–Landau equation). Building upon the seminal works on the nonlinear Poiseuille configuration (Stuart 1960; Stewartson & Stuart 1971), by means of a multiple scaling approach, we are confident that explicit results can be retrieved in our context. Such analysis being beyond the scope of the current paper, we leave this future study for a separate article.

Acknowledgments

Centre de Calcul Intensif d'Aix-Marseille is acknowledged for granting access to its high-performance computing resources.

Funding

This work received support from the French government under the France 2030 investment plan, as part of the Initiative d'Excellence d'Aix-Marseille Université - A*MIDEX (AMX-19-IET-010). This work was granted access to the HPC resources of IDRIS under the allocation 2022-A0120407543 made by GENCI.

Declaration of interests

The authors report no conflict of interest.

REFERENCES

Bakas, N. A. & Farrell, B. F. 2009*a* Gravity waves in a horizontal shear flow. part i : Growth mechanisms in the absence of potential vorticity perturbations. *J. Phys. Oceano.* **39**, 481–496.

Bakas, N. A. & Farrell, B. F. 2009*b* Gravity waves in a horizontal shear flow. part ii : Interaction between gravity waves and potential vorticity perturbations. *J. Phys. Oceano.* **39**, 497–511.

Basovich, A. Y. & Tsimring, L. S. 1984 Internal waves in a horizontally inhomogeneous flow. *J. Fluid Mech.* **142**, 223–249.

Billant, P. & Chomaz, J. M. 2000 Theoretical analysis of the zigzag instability of a vertical columnar vortex pair in a strongly stratified fluid. *J. Fluid Mech.* **419**, 29–63.

Brethouwer, G., Billant, P., Lindborg, E. & Chomaz, J. M. 2007 Scaling analysis and simulation of strongly stratified turbulent flows. *J. Fluid Mech.* **585**, 343–368.

Burke, J. & Knobloch, E. 2007 Homoclinic snaking: structure and stability. *Chaos* **17** (3), 037102.

Cairns, R. A. 1979 The role of negative energy waves in some instabilities of parallel flows. *J. Fluid Mech.* **92** (1), 1–14.

Carpenter, J. R., Tedford, W., E., Heifetz, E. & Lawrence, G. A. 2011 Instability in stratified shear flow: review of a physical interpretation based on interacting waves. *Appl. Mech. Rev.* **64** (6), 060801.

Caulfield, C. P. 1994 Multiple linear instability of layered stratified shear flow. *J. Fluid Mech.* **258**, 255–285.

Caulfield, C. P. 2021 Layering, instabilities, and mixing in turbulent stratified flows. *Annu. Rev. Fluid Mech.* **53**, 113–145.

Chen, J. 2016 Stabilité d'un écoulement stratifié sur une paroi et dans un canal. PhD thesis, Aix Marseille Université.

Crawford, J. D. & Knobloch, E. 1991 Symmetry and symmetry-breaking bifurcations in fluid dynamics. *Annu. Rev. Fluid Mech.* **23**, 341–387.

Facchini, G., Favier, B., Le Gal, P., Wang, M. & Le Bars, M. 2018 The linear instability of the stratified plane couette flow. *J. Fluid Mech.* **853**, 205–234.

Fischer, P. F. 1997 An overlapping schwarz method for spectral element solution of the incompressible navier–stokes equations. *J. Comput. Phys.* **133** (1), 84–101.

Fischer, P. F., Loth, F., Lee, S. E., Lee, S. W., Smith, D. S. & Bassiouny, H. S. 2007 Simulation of high-reynolds number vascular flows. *Comput. Methods Appl. Mech. Eng.* **196** (31–32), 3049–3060.

Gage, K. S. & Reid, W. H. 1968 The stability of thermally stratified plane poiseuille flow. *J. Fluid Mech.* **33** (1), 21–32.

Gibson, J. F. & Schneider, T. M. 2016 Homoclinic snaking in plane couette flow: bending, skewing and finite-size effects. *J. Fluid Mech.* **794**, 530–551.

Howard, L. N. 1961 Note on a paper of John W. Miles. *J. Fluid Mech.* **10** (4), 509–512.

Labarbe, J. & Kirillov, O. N. 2020 Membrane flutter induced by radiation of surface gravity waves on a uniform flow. *J. Fluid Mech.* **901**, A4.

Le Bars, M. & Le Gal, P. 2007 Experimental analysis of the stratorotational instability in a cylindrical Couette flow. *Phys. Rev. Lett.* **99**, 064502.

Le Dizès, S. & Billant, P. 2009 Radiative instability in stratified vortices. *Phys. Fluids* **21** (9), 096602.

Le Dizès, S. & Riedinger, X. 2010 The strato-rotational instability of Taylor–Couette and Keplerian flows. *J. Fluid Mech.* **660**, 147–161.

Le Gal, P., Harlander, U., Borcia, I. D., Le Dizès, S., Chen, J. & Favier, B. 2021 Instability of vertically stratified horizontal plane Poiseuille flow. *J. Fluid Mech.* **907**.

Lindborg, E. 2006 The energy cascade in a strongly stratified fluid. *J. Fluid Mech.* **550**, 207–242.

Lucas, D., Caulfield, C. P. & Kerswell, R. R. 2017 Layer formation in horizontally forced stratified turbulence: connecting exact coherent structures to linear instabilities. *J. Fluid Mech.* **832**, 409–437.

Lucas, D., Caulfield, C. P. & Kerswell, R. R. 2019 Layer formation and relaminarisation in plane couette flow with spanwise stratification. *J. Fluid Mech.* **868**, 97–118.

Miles, J. W. 1961 On the stability of heterogeneous shear flows. *J. Fluid Mech.* **10** (4), 496–508.

Molemaker, M. J., McWilliams, J. C. & Yavneh, I. 2001 Instability and equilibration of centrifugally stable stratified Taylor–Couette flow. *Phys. Rev. Lett.* **86**, 5270–5273.

Oglethorpe, R. L. F., Caulfield, C. P. & Woods, A. W. 2013 Spontaneous layering in stratified turbulent taylor–couette flow. *J. Fluid Mech.* **721**, R3.

Orszag, S. A. 1971 Accurate solution of the orr–sommerfeld stability equation. *J. Fluid Mech.* **50** (4), 689–703.

Park, J. & Billant, P. 2013 The stably stratified Taylor–Couette flow is always unstable except for solid-body rotation. *J. Fluid Mech.* **725**, 262–280.

Riedinger, X., Le Dizès, S. & Meunier, P. 2011 Radiative instability of the flow around a rotating cylinder in a stratified fluid. *J. Fluid Mech.* **672**, 130–146.

Sakai, S. 1989 Rossby-kelvin instability: a new type of ageostrophic instability caused by a resonance between rossby waves and gravity waves. *J. Fluid Mech.* **202**, 149–176.

Satomura, T. 1981 An investigation of shear instability in a shallow water. *J. Met. Soc. Japan* **59** (1), 148–167.

Schlichting, H. 1933 Berechnung der Anfachung kleiner Störungen bei der Plattenströmung. *ZAMM* **13**, 171–174.

Schneider, T. M., Gibson, J. F. & Burke, J. 2010 Snakes and ladders: localized solutions of plane couette flow. *Phys. Rev. Lett.* **104** (10), 104501.

Stewartson, K. & Stuart, J. T. 1971 A non-linear instability theory for a wave system in plane poiseuille flow. *J. Fluid Mech.* **48** (3), 529–545.

Stuart, J. T. 1960 On the non-linear mechanics of wave disturbances in stable and unstable parallel flows part 1. the basic behaviour in plane poiseuille flow. *J. Fluid Mech.* **9** (3), 353–370.

Taylor, J. R., Deusebio, E., Caulfield, C. P. & Kerswell, R. R. 2016 A new method for isolating turbulent states in transitional stratified plane couette flow. *J. Fluid Mech.* **808**, R1.

Tollmien, W. 1929 Über die entstehung der turbulenz. *Nachr. Ges. Wiss. Göttingen* pp. 21–24.

Yang, A. J., Tedford, E. W., Olsthoorn, J., Lefauve, A. & Lawrence, G. A. 2022 Reynolds stresses in holmboe instabilities: From linear growth to saturation. *arXiv:2103.12220* .

Zhou, Q., Taylor, J. R. & Caulfield, C. P. 2017*a* Self-similar mixing in stratified plane couette flow for varying prandtl number. *J. Fluid Mech.* **820**, 86–120.

Zhou, Q., Taylor, J. R., Caulfield, C. P. & Linden, P. F. 2017*b* Diapycnal mixing in layered stratified plane couette flow quantified in a tracer-based coordinate. *J. Fluid Mech.* **823**, 198–229.